ACS MATERIALS LETTERS

www.acsmaterialsletters.org

LETTER

$InGaZnO_4$ and In_2O_3 Mobility Trend: The Role of Structural Disorder from Amorphous to Crystalline States

Hyeongjun Jang,[#] Taehyun Kim,[#] Wonsok Lee, Minhee Cho, Daewon Ha, Muhammad A. Alam, Peide D. Ye, and Changwook Jeong*

Cite This: *ACS Materials Lett.* 2025, 7, 2024−2030

Read Online

ACCESS | Metrics & More | Article Recommendations | Supporting Information

ABSTRACT: **This study investigates the mobility trends of indium−gallium−zinc oxide (IGZO) thin-film transistors over a wide range of fabrication conditions, from amorphous to crystalline phases. By utilizing machine learning potential (MLP) to generate 70 distinct IGZO structures, we analyze electron mobility while taking into account structural disorder and electron scattering mechanisms. Our findings reveal that mobility peaks at the transition from amorphous to nanocrystalline phases, and then, as more ordered, crystalline structures emerge, the mobility decreases sharply due to the distortion of polyhedron of indium−oxygen in well-ordered regions. These results offer critical insights into optimizing the fabrication conditions for high-performance IGZO devices by identifying the ideal structural phase for achieving maximum mobility.**

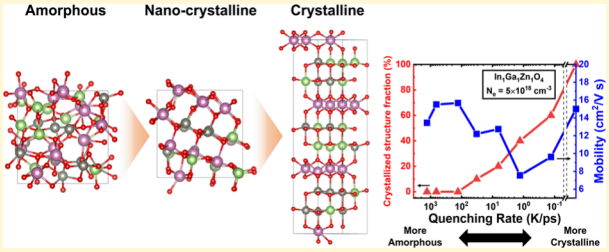

An amorphous IGZO (a-IGZO) is attracting attention as a promising alternative to the silicon (Si) channel due to its high mobility, low off-state leakage current, and good uniformity over large areas.[1] To utilize IGZO as a channel material, we need to address stability and reliability issues and achieve a positive threshold voltage with high mobility. In general, IGZO with high oxygen vacancy density results in a high carrier concentration and hence higher mobility. However, this also leads to problems such as negative threshold voltage and reduced stability and reliability due to high defect density. Therefore, to ensure that IGZO solves these problems while maintaining high mobility, mobility enhancement must be achieved by means other than increasing the carrier concentration.

The electronic performance of IGZO varies significantly depending on the fabrication conditions, such as the degree of structural disorder and defect density change. In particular, both enhancements and degradations in mobility due to variations in substrate temperature, oxygen rate, and postannealing process have been reported experimentally.[2−9] Most studies suggest that the reasons for these mobility trends by fabrication conditions are changes in carrier concentration or grain boundary scattering. But these reasons cannot explain sufficiently the fluctuation of mobility since there are cases where carrier concentration and grain boundary scattering are not directly correlated with the mobility.[2−9] In addition, the influence of grain boundary scattering in C-axis Aligned Crystalline (CAAC) IGZO is minimal.[1]

Changes in structural disorder play a crucial role in determining mobility in addition to variations in carrier concentration and grain boundary scattering. Therefore, achieving optimal mobility hinges on understanding how structural disorder, driven by fabrication conditions, impacts electron transport. In this study, machine learning potential (MLP) is developed to generate a-IGZO structures, ranging from amorphous to crystalline phases. Then the impurity density induced by structural disorder is obtained via ab initio simulation to calculate the mobility for these structures. By focusing on the influence of electron scattering induced by structural disorder, we identified key trends in mobility. Our findings reveal a peak in mobility at the transition point between amorphous and nanocrystalline phases, followed by a sharp decrease in mobility in more ordered crystalline regions due to the distortion of the In−O polyhedron. This investigation offers critical insights into the fabrication

Received: February 18, 2025
Revised: April 24, 2025
Accepted: April 24, 2025

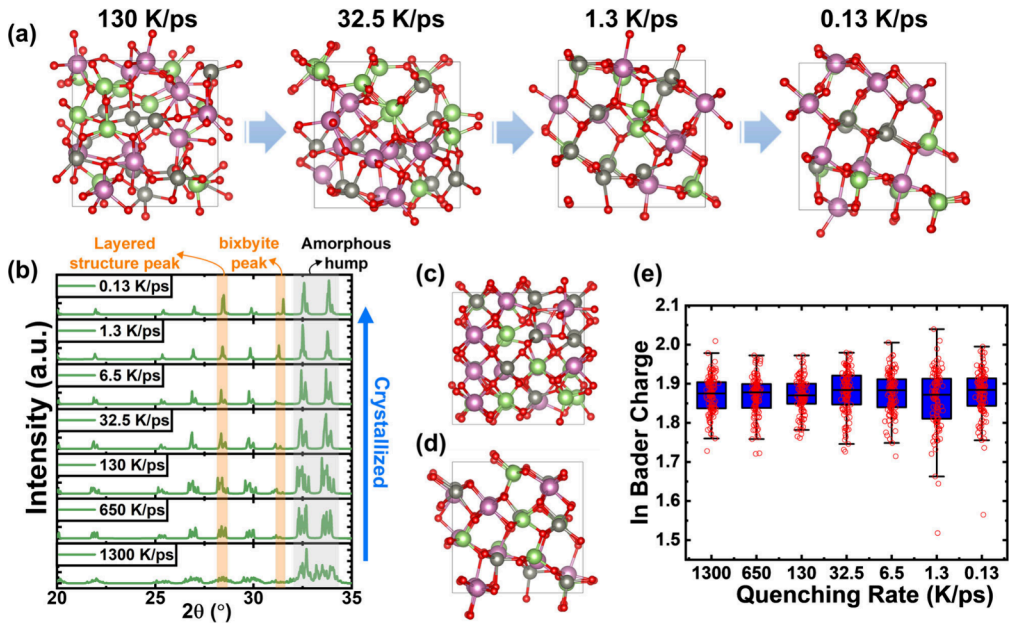

Figure 1. (a) Four structures at quenching rates of 130, 32.5, 1.3, and 0.13 K/ps, respectively. It can be observed that the structures become layered structures. (b) The XRD simulation for each quenching rate. Peak widths of lower quenching rate structures are narrower than those of higher quenching rate structures. (c) Bixbyite-like structure and (d) layered-like structure generated at 1.3 or 0.13 K/ps. (e) Indium (In) Bader charges and their distribution at each quenching rate for IGZO. Each of the red circles represents the Bader charge value of a single indium atom.

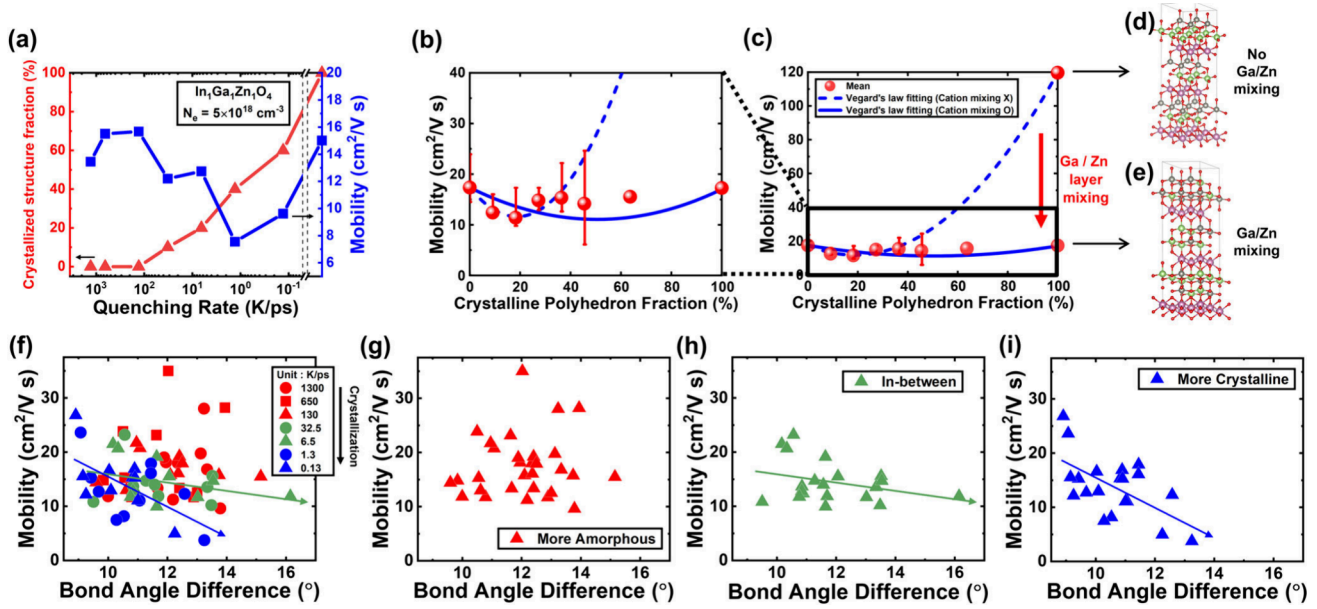

Figure 2. (a) IGZO mobility trend and crystalline structure fraction as a function of quenching rate. The mobility is calculated at a carrier concentration of 5×10^{18} cm^{-3}. The marker on the right *y*-axis represents the result of C-Axis Aligned Crystalline (CAAC) IGZO. (b, c, d, e) The relationship between the number of crystalline-like polyhedra and mobility. The U-shaped curve is observed when fitted using Vegard's law. (b) is a enlarged version of (c) with a reduced *y*-axis range to emphasize the U-shaped trend. In crystalline IGZO, due to the mixing of Ga and Zn ions, the U-shaped curve of the blue dashed line becomes the U-shaped curve of the blue solid line. (d) and (e) represent CAAC IGZO structures without and with Ga/Zn layer mixing, respectively. (f) The reason for the mobility trend from amorphous to crystalline phase for IGZO. The relationship between In−O bond angle difference (BAD) and mobility for all 70 structures. BAD is a measure of the degree of distortion in the polyhedron. The amount of In−O BAD decreases as structures transition to a crystalline phase. The relationship between In−O BAD and mobility in (g) more-amorphous phases, (h) in-between phases, and (i) in more-crystalline phases. The influence of In−O BAD on mobility becomes more pronounced as crystallization progresses. A total of 30, 20, and 20 data points are used for (g), (h), and (f), respectively. The lines with arrows indicate linear fits of each data set, and the corresponding Pearson correlation coefficients are provided to quantify the strength of these correlations. The Pearson correlation coefficients are 0, −0.32, and −0.60, respectively, showing a progressive strengthening of the correlation.

https://doi.org/10.1021/acsmaterialslett.5c00348
ACS Materials Lett. 2025, 7, 2024−2030

strategies necessary for optimizing IGZO thin-film transistors (TFTs) and suggests an ideal phase for maximizing the performance.

By melting the crystalline IGZO structure and then quenching it at different quenching rates, it is possible to obtain structures with different degrees of structural disorder. As the quenching rate decreases, there are many opportunities for atoms to find a more stable configuration because the structure takes a long time to quench. Therefore, structural disorder decreases and more ordered structures appear. Figure 1 (a) visually illustrates the process of crystallization. As the quenching rate decreases from 130 to 0.13 K/ps, the disorder gradually declines. An ordered arrangement begins to appear at 32.5 K/ps, and a distinct ordered structure is observed at 1.3 K/ps. At 0.13 K/ps, the arrangement is well-ordered not only globally but also locally. Figure 1 (b) shows X-ray diffraction (XRD) simulation of a-IGZO structures at each quenching rate. As quenching rate decreases, XRD peaks corresponding to the bixbyite and layered structure emerge, and most peaks become narrower at lower quenching rates in XRD simulation. The atomic configurations of bixbyite- or layered- structure are represented in Figure 1 (c), (d), respectively. Based on the results from Figure 1 (a) and (b), at quenching rates below about 100 K/ps, structures emerge that are not perfectly crystalline but show some degree of alignment. Therefore, it can be assumed that the nanocrystalline structure is generated at below about 100 K/ps.

These structures, with varying crystallinity, are used to study how structural disorder is related to mobility. To assess the effect of structural disorder on mobility in a-IGZO structures with different crystallinities, it is essential to accurately calculate the Bader charge for each atom. For the 70 structures generated by MLP, the Bader charge of all of the atoms is computed by ab initio calculations. To improve the accuracy of Bader charge calculations, the charge density is computed on a fine real-space grid consisting of 200 million mesh points. The detailed explanation and computation of the Bader charge are provided in the Supporting Information section 2. For example, the distributions of Bader charges of Indium (In) are shown in Figure 1 (e). Although the structural phase changes with the quenching rate, the average value of Bader charges remains nearly constant, while only the deviation varies. The calculated Bader charges are used to calculate the impurity density induced by structural disorder, ρ_{SD}, which is determined from the variance of the Bader charge and the volume of the unit cell. The mobility at each quenching rate is then calculated based on ρ_{SD} by solving the Boltzmann transport equation with relaxation time approximation, accounting for both Polar Optical Phonon (POP) and Ionized Impurity (II) scattering.

The IGZO mobility trend by quenching rates is shown in Figure 2 (a). The data point at the far-right corner of the figure represents the highly ordered CAAC structure. In this structure, we consider the mixing of Ga and Zn cations in the Ga/Zn layers. Initially, at a high quenching rate, as the quenching rate decreases, the structural disorder of the amorphous structures is reduced, leading to increased mobility. Thus, at a quenching rate of 130 K/ps, the mobility is at its maximum. However, below a quenching rate of 100 K/ps, crystallized structures such as layered or bixbyite coexist with the amorphous structure, leading to an increased variance in Bader charges and decreased mobility. Therefore, the mobility reaches a minimum value at a quenching rate of 1.3K/ps. Beyond these points, as more crystallized structures form, the mobility increases and reaches high values in the CAAC structure.

Identifying the reasons for the mobility degradation as the structure transitions from amorphous to crystalline and the subsequent increase in mobility once sufficient crystallization occurs provides valuable insight into finding the optimal structural phase. To identify these reasons, coordination number (CN), bond length, and bond angle are investigated for all atoms in each structure. Using these three parameters, we define the metal−oxygen polyhedron and find the reason for the mobility trend from the In−O polyhedron analysis. The In−O polyhedron analysis is composed of two primary processes: (1) the enumeration of a crystalline-like polyhedron (c-polyhedron) and (2) the calculation of In−O bond angle differences (BAD) in each polyhedron.

Figure 2 (b) and (c), the result of enumeration of c-polyhedron process, illustrates the relationship between the number of crystalline-like polyhedron and mobility. Mobility decreases with an increasing fraction of c-polyhedron but subsequently improves once the fraction reaches a sufficiently high value, exhibiting a U-shaped curve when fitted with Vegard's law. To comprehend the reason for the U-shaped behavior of mobility as a function of the crystalline phase fraction, we next conducted an analysis through the calculation of the In−O BAD. The procedure is as follows: First, we classify all In−O polyhedra in each structure into octahedral (CN = 6), trigonal bipyramidal (CN = 5), and tetragonal (CN = 4). Second, all In−O bond angles within the In−O polyhedron are calculated. Third, we calculate the differences between all of these bond angles and those of the perfect polyhedron determined by CN. This approach provides a measure of how much the polyhedron is distorted compared to the perfect polyhedron structure. The distortion of the In−O polyhedron substantially affects the Bader charge distribution and, therefore, the mobility.

In Figure 2 (g), there is no correlation between the In−O BAD and the mobility for the structures closer to the amorphous phase. However, as crystallization proceeds, the correlation between the In−O BAD and mobility begins to emerge, as shown in Figure 2 (h). As the structure approaches the more crystalline phase, as shown in Figure 2 (i), the correlation strengthens. These results show that the distortion of the In−O polyhedron decreases the mobility in more-crystalline phase. In other words, in the presence of a crystalline phase, the distortion of the In−O polyhedron leads to mobility degradation. This occurs because, in a more-crystalline structure with an increased long-range order length shown as Figure S3, the atomic bonds are connected in a regular pattern, so differences in In−O bond angles affect the overall structure and thus the mobility. In contrast, in the amorphous structure, the atomic bonds are flexible, so BADs do not significantly affect the mobility. Therefore, in the amorphous phase, where the influence of BAD is negligible, structural disorder decreases as crystallization proceeds, leading to an increase in mobility. However, in the nano-crystalline phase, where the influence of BAD becomes more significant as crystallinity increases, mobility decreases even though the structural disorder is reduced.

In Figure 2 (f), it can be observed that the effect of the In−O BAD on mobility intensifies as crystallization proceeds, while the amount of In−O BAD itself decreases. Once the structures are sufficiently crystallized and the effect of the In−

https://doi.org/10.1021/acsmaterialslett.5c00348
ACS Materials Lett. 2025, 7, 2024−2030

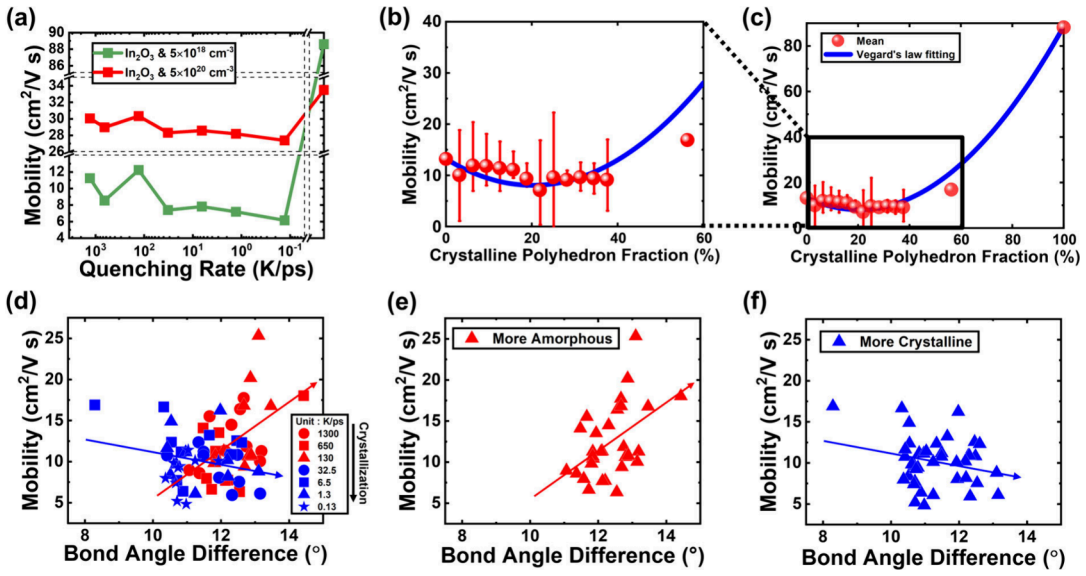

Figure 3. (a) The trend of In_2O_3 mobility as a function of quenching rate. The mobility is calculated at carrier concentrations of 5×10^{18} cm^{-3} and 5×10^{20} cm^{-3}. The marker on the right *y*-axis represents the result of perfect crystalline In_2O_3. (b, c) The relationship between the number of crystalline-like polyhedron and mobility and U-shaped curve when fitted with Vegard's law. (b) is a enlarged version of (c) with a reduced *x*-axis and *y*-axis range to emphasize the U-shaped trend. (d) The reason for the mobility trend from amorphous to crystalline phase for In_2O_3. The relationship between In−O BAD and mobility for all 70 In_2O_3 structures. The relationship between In−O BAD and mobility (e) in more-amorphous phases and (f) in more-crystalline phases. A total of 30 and 40 data points are used for (e) and (f), respectively. The lines with arrows indicate linear fits of each data set, and the corresponding Pearson correlation coefficients are provided to quantify the strength of these correlations. The Pearson correlation coefficients are −0.25, +0.48, respectively. It shows an opposite correlation between (e) and (f). The relatively low correlation coefficient in the (e) is presumed to result from the lack of data in areas with small bond angle difference.

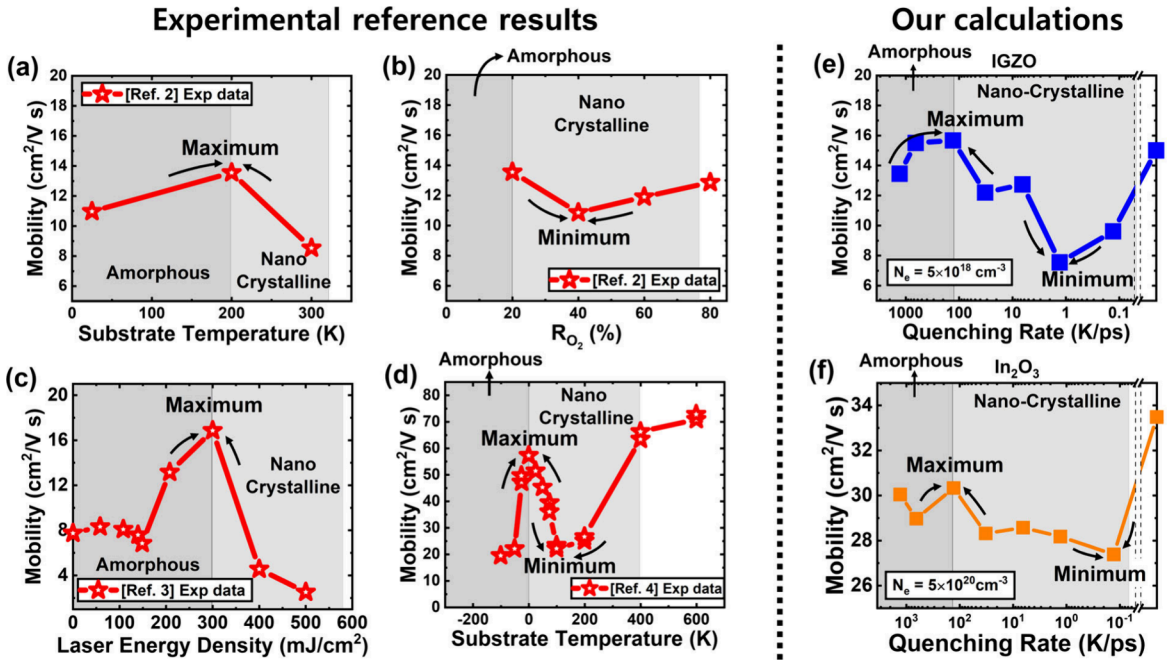

Figure 4. Experimentally, the mobility trend shows a maximum at the structure transition from amorphous to nanocrystalline and minimum at nanocrystalline. The amorphous and nanocrystalline regions are defined by XRD data in each Reference. (a, b) The experimental data of IGZO mobility depending on substrate temperature and oxygen rate from ref 2. (c) The Hall mobility values of IGZO in ref 3 depending on laser energy density during excimer laser annealing. (d) The experimental data of In_2O_3 mobility depending on substrate temperature from ref 4. Our calculations for (e) IGZO and (f) In_2O_3 show the mobility maximum and minimum in regions consistent with the experimental results. The amorphous and nanocrystalline regions are defined by XRD simulations and the proportion of crystalline structures.

O BAD on mobility stabilizes and the amount of In−O BAD gradually decreases, the mobility increases. Thus, after the phase transition from amorphous to nanocrystalline, the mobility decreases up to 1.3 K/ps and increases at 0.13 K/ps.

https://doi.org/10.1021/acsmaterialslett.5c00348
ACS Materials Lett. 2025, 7, 2024−2030

The same calculation is also performed for In_2O_3, which is one of the representative materials in AOS, such as IGZO. Figure 3 (a) shows the mobility trend of In_2O_3 at different quenching rates. In the red curve in Figure 3 (a), since the carrier concentration is sufficiently high, the electrons are not affected by the impurity induced by the structural disorder. Thus, POP and II scattering are dominant, and the mobility does not change significantly depending on the quenching rate. On the other hand, in the green curve, there is a noticeable change in mobility depending on the quenching rate due to the relatively low carrier concentration. In the perfect crystalline structure of In_2O_3, the mobility increases up to ~90 $cm^2/(V{\cdot}s)$ because there is no structural disorder and weak POP and II scattering due to low carrier concentrations. Similar to IGZO, In_2O_3 exhibits a gradual decrease in its mobility as structures crystallize. Mobility has a maximum at a quenching rate of 130 K/ps and undergoes degradation at rates below 130 K/ps.

In Figure 3 (b) and (c), the U-shaped curve is observed, consistent with that of IGZO. In addition, the mechanism that causes mobility degradation during the crystallization in In_2O_3 is similar to the one found in IGZO. In Figure 3 (e), the mobility tends to increase with larger BAD in the amorphous phase. However, as the structure approaches a more crystalline form, there is a decrease in mobility with increasing BAD as shown in Figure 3 (f). In contrast to the a-IGZO, the reduction in BAD is not significant in the more-crystalline regions, and thus, the mobility does not show a tendency to increase again. However, in a perfectly crystalline structure, BAD is almost absent, resulting in minimal Bader charge differences and high mobility.

To sum up these results of the mobility trend for IGZO and In_2O_3, the mobility does not consistently increase as structural disorder decreases. Unexpectedly, the mobility degradation occurs during the phase transition from amorphous to crystalline. This can be explained by the fact that in amorphous phase, the lack of long-range order means that even if BAD is present, it does not significantly affect the overall structure. In contrast, in crystalline structures, where the arrangement is well ordered, BAD has a considerable effect on the overall structure, leading to a large Bader charge difference. As a result, mobility has maximum and minimum values in certain regions and does not change monotonically with structural disorder. This trend is observed similarly for both IGZO and In_2O_3.

The tendency for the mobility to degrade and have maximum and minimum values depending on the structural disorder is observed in experiments where fabrication conditions, such as the substrate temperature or oxygen flow rate, are modified to improve the atomic arrangement in the structure. In Figure 4 (a), (b), the experimental data of IGZO TFTs from ref 2 show that increasing the substrate temperature or the oxygen rate during the fabrication process results in a more crystalline structure, which in turn affects the mobility performance. In these experiments, it can be observed that the mobility reaches its maximum value at the phase transition from amorphous to nanocrystalline and exhibits a minimum within the nanocrystalline region. In Figure 4 (c), during the excimer laser annealing, the mobility also shows the same trend, reaching a maximum at the phase transition from amorphous to nanocrystalline.[3] Similarly, the experimental results for In_2O_3 also show a mobility degradation during the crystallization process from the amorphous to the crystalline phase, with the mobility having both maximum and minimum values shown as in Figure 4 (d).[4] In Figure 4 (e), (f), our simulation results are consistent with the experimental results that mobility does not change monotonically with fabrication conditions but rather exhibits maximum and minimum values in specific regions.

Here, we provide an insight into the mobility trend of IGZO and In_2O_3 from the amorphous to crystalline phase. The mobility degradation that occurs during the transition from amorphous to crystalline phases, as observed experimentally, is reproduced in our simulations and its causes are identified. From the information on the phases where mobility reaches its maximum and minimum values, structures to avoid and optimal structures to achieve high mobility can be proposed.

This work investigates the mobility behavior of IGZO and In_2O_3 as they transition from amorphous to crystalline phases. By generating structures using MLP and calculating the mobility based on electron scattering mechanisms, we demonstrate how structural disorder plays a pivotal role in determining mobility. We show that reducing disorder through optimized fabrication conditions enhances mobility but excessive crystallinity leads to a decline in performance. To elucidate the cause of the decrease in mobility, we investigate the coordination number, bond length, and bond angle for all atoms in each structure. This analysis shows that the distortion of the In−O polyhedron in the more-crystalline phase is responsible for the decrease in mobility. Based on these results, the same calculations are carried out for In_2O_3, revealing a comparable trend in the results. Ultimately, our study pinpoints the optimal structural phase at the boundary between the amorphous and crystalline phases for achieving high mobility in IGZO TFTs. These findings provide valuable guidance for tailoring fabrication processes to improve the IGZO-based device performance.

COMPUTATIONAL METHODS

The atomic structures of amorphous oxides are generated from the melt-quenching process by using molecular dynamic (MD) simulations. The MLP is essentially required to obtain crystalline-like structures via quenching MD simulations, especially at a rate below 6.5 K/ps. The MLP based on equivariant graph neural network is chosen to reduce the number of required structural features, in which forces can be efficiently trained for amorphous and multielement systems.[10,11] The training data is produced by performing ab initio MD simulation at the near-melting temperature of ~2300 K, since it is known that the dynamics of short-range interacting amorphous material is obeyed by the locally ordered configuration.[12] To reflect the changes in structural disorder as a function of fabrication conditions, 10 different structures are generated at 7 different quenching rates, 1300, 650, 130, 32.5, 6.5, 1.3, and 0.13 K/ps. More detailed information on the MLP and MD simulation is given in the Supporting Information section 1.[21]

In a-IGZO structures, structural disorder induces fluctuations of conduction band (CB) states, i.e., band percolation. And these fluctuations are barriers or impurities for electron transport. Therefore, it is important to consider these structural disorder induced fluctuations to accurately calculate mobility of IGZO. To do this, we model the electron's scattering caused by these fluctuations by calculating the Bader charge for all atoms in each structure. The differences in Bader charges between identical cations can be interpreted as the presence of impurities, with charges corresponding to these

https://doi.org/10.1021/acsmaterialslett.5c00348
ACS Materials Lett. 2025, 7, 2024−2030

differences. Therefore, from the Coulomb scattering formula, we define structural disorder scattering as

$$\frac{1}{\tau_{SD}(k)} = \sum_{k'} \frac{2\pi}{\hbar} \frac{e^4 \rho_{SD}}{\varepsilon_s^2} \frac{\delta(E' - E)}{|k' - k|^2 + \left(\frac{1}{L_s}\right)^2} \times \frac{k'}{k}(1 - \cos\alpha) \quad (1)$$

where L_s is Debye length, ε_s is dielectric constant and ρ_{SD} represents the impurity density induced by structural disorder.[13,14] To determine ρ_{SD}, the impurity charge and density must be defined. Since the impurity charge is the difference in Bader charges between identical cations and the impurity density is the number of cations in the unit cell divided by the unit cell volume, we define the impurity density induced by structural disorder as

$$\rho_{SD} \equiv \sum_{j=In,Ga,Zn} \sum_{i=1}^{n_j} \frac{\{Z_{i,j}^X - Z_{i,j}^Y\}^2}{V} = \sum_{j=In,Ga,Zn} \sum_{i=1}^{n_j} \frac{2\sigma^2}{V} \quad (2)$$

where Z^x and Z^y are randomly selected Bader charge values from among all calculated Bader charge values in 10 structures per each quenching rate point, V represents the volume of the unit cell, and the n_j represents the number of cations of type j. Since the mean of $\{Z_{i,j}^X - Z_{i,j}^Y\}^2$ is equal to the mean of $2\{Z_{i,j}^{amor} - Z_j^{avg}\}^2$, we substitute $\{Z_{i,j}^X - Z_{i,j}^Y\}^2$ with twice the variance ($2\sigma^2$). From eq 2, it is obvious that the standard deviation of Bader charges for each cation is significantly related to impurity density. Further details and validation of our modeling of electron scattering induced by structural disorder are provided in the Supporting Information section 5.

In addition, the POP scattering and II scattering caused by lattice vibration and oxygen vacancies are considered[13−20]. The POP scattering rate is

$$\frac{1}{\tau_{POP}(k)} = \sum_{k'} \frac{2\pi}{\hbar} \frac{e^2 \rho_m \omega_0^2}{\beta^2 \varepsilon_s \varepsilon_0} \cdot \left(\frac{\varepsilon_0}{\varepsilon_\infty} - 1\right) \cdot \frac{\hbar}{2\rho_m V\omega} \times \left(N_\omega + \frac{1}{2} \pm \frac{1}{2}\right)\delta(E' - E \pm \hbar\omega(\beta)) \quad (3)$$

and II scattering rate is

$$\frac{1}{\tau_{II}(k)} = \sum_{k'} \frac{2\pi}{\hbar} \frac{e^4 N_e}{\varepsilon_s^2 V} \frac{\delta(E' - E)}{|k' - k|^2 + \left(\frac{1}{L_s}\right)^2} \times \frac{k'}{k}(1 - \cos\alpha) \quad (4)$$

where ω is optical phonon energy, ρ_m is mass density, β is phonon wavevector, ε_∞ is high frequency dielectric constant, and N_e is carrier concentration.

In these three electron scattering calculations, the electronic band structure is based on the effective mass approximation, where the effective mass is set to $0.25m_e$.[1,13] This approximation is chosen to simplify the treatment of electronic states while maintaining reasonable accuracy for the mobility calculation. The scattering rate calculations are performed using an in-house code, which is based on the methodology outlined in ref 14.

■ ASSOCIATED CONTENT

Supporting Information

The Supporting Information is available free of charge at https://pubs.acs.org/doi/10.1021/acsmaterialslett.5c00348.

(1) Details of machine learning potential, (2) explanation and computation of Bader charge, (3) length of long-range order length, (4) carrier concentration vs mobility in crystalline In_2O_3, and (5) discussion of modeling the effect of structural disorder on mobility using Bader charge analysis and Coulombic scattering mechanisms (PDF)

■ AUTHOR INFORMATION

Corresponding Author

Changwook Jeong − *Graduate School of Semiconductor Materials and Devices Engineering, Ulsan National Institute of Science and Technology, Ulsan 44919, Republic of Korea*; Email: changwook.jeong@unist.ac.kr

Authors

Hyeongjun Jang − *Graduate School of Semiconductor Materials and Devices Engineering, Ulsan National Institute of Science and Technology, Ulsan 44919, Republic of Korea*; orcid.org/0009-0003-1455-7395

Taehyun Kim − *Graduate School of Semiconductor Materials and Devices Engineering, Ulsan National Institute of Science and Technology, Ulsan 44919, Republic of Korea*; orcid.org/0009-0009-0414-1226

Wonsok Lee − *Advanced Device Research Lab, Semiconductor R&D Center, Samsung Electronics, Suwon 16677, Republic of Korea*

Minhee Cho − *Advanced Device Research Lab, Semiconductor R&D Center, Samsung Electronics, Suwon 16677, Republic of Korea*

Daewon Ha − *Advanced Device Research Lab, Semiconductor R&D Center, Samsung Electronics, Suwon 16677, Republic of Korea*

Muhammad A. Alam − *School of Electrical and Computer Engineering, Purdue University, West Lafayette, Indiana 47907, United States*; orcid.org/0000-0001-8775-6043

Peide D. Ye − *School of Electrical and Computer Engineering, Purdue University, West Lafayette, Indiana 47907, United States*; orcid.org/0000-0001-8466-9745

Complete contact information is available at: https://pubs.acs.org/10.1021/acsmaterialslett.5c00348

Author Contributions

#H. Jang and T. Kim contributed equally to this work. The manuscript was written through contributions of all authors. All authors have given approval to the final version of the manuscript.

Notes

The authors declare no competing financial interest.

■ ACKNOWLEDGMENTS

This work was supported by the National Research Foundation of Korea (NRF), funded by the Ministry of Science and ICT (MSIT) (RS-2024-00408180, RS-2023-00257666, RS-2024-00458251); the Technology Innovation Program (RS-2023-00231956/P0023703), funded by MOTIE; the IITP grant (No. RS-2020-II201336, AIGS), funded by

MSIT; the research project fund (1.230063.01) of UNIST; and Samsung Electronics.

■ ABBREVIATIONS

IGZO, indium−gallium−zinc oxide; MLP, machine learning potential; a-IGZO, amorphous IGZO; Si, silicon; CAAC, C-axis aligned crystalline; TFTs, thin-film transistors; XRD, X-ray diffraction; In, indium; POP, polar optical phonon; II, ionized impurity; MD, molecular dynamic; CN, coordination number; c-polyhedron, crystalline-like polyhedron; BAD, bond angle difference; CB, conduction band

■ REFERENCES

(1) Kimizuka, N.; Yamazaki, S. *Physics and Technology of Crystalline Oxide Semiconductor CAAC-IGZO: Fundamentals*. John Wiley & Sons, 2016.

(2) Glushkova, A. V.; Dekkers, H. F. W.; Nag, M.; del Agua Borniquel, J. I.; Ramalingam, J.; Genoe, J.; Heremans, P.; Rolin, C. Systematic Study on the Amorphous, C-Axis-Aligned Crystalline, and Protocrystalline Phases in In−Ga−Zn Oxide Thin-Film Transistors. *ACS Applied Electronic Materials* **2021**, *3*, 1268−1278.

(3) Nakata, M.; Takechi, K.; Eguchi, T.; Tokumitsu, E.; Yamaguchi, H.; Kaneko, S. Flexible High-Performance Amorphous $InGaZnO_4$ Thin-Film Transistors Utilizing Excimer Laser Annealing. *Jpn. J. Appl. Phys.* **2009**, *48*, 081607.

(4) Buchholz, D. B.; Ma, Q.; Alducin, D.; Ponce, A.; Jose-Yacaman, M.; Khanal, R.; Medvedeva, J. E.; Chang, R. P. H. The Structure and Properties of Amorphous Indium Oxide. *Chem. Mater.* **2014**, *26*, 5401−5411.

(5) Suko, A.; Jia, J.; Nakamura, S.; Kawashima, E.; Utsuno, F.; Yano, K.; Shigesato, Y. Crystallization Behavior of Amorphous Indium−Gallium−Zinc-Oxide Films and its Effects on Thin-Film Transistor Performance. *Japanese journal of applied physics* **2016**, *55*, 035504.

(6) Kang, Y.; Lee, W.; Kim, J.; Keum, K.; Kang, S.-H.; Jo, J.-W.; Park, S. K.; Kim, Y.-H. Effects of Crystalline Structure of IGZO Thin Films on the Electrical and Photo-Stability of Metal-Oxide Thin-Film Transistors. *Mater. Res. Bull.* **2021**, *139*, 111252.

(7) Lee, M.; Dho, J. Controlling the Electrical and the Optical Properties of Amorphous IGZO Films Prepared by Using Pulsed Laser Deposition. *J. Korean Phys. Soc.* **2011**, *58*, 492−497.

(8) Xu, W.; Jiang, J.; Xu, S.; Zhang, Y.; Xu, H.; Han, L.; Feng, X. Effect of Substrate Temperature on Sputtered Indium-Aluminum-Zinc Oxide Films and Thin Film Transistors. *J. Alloys Compd.* **2019**, *791*, 773−778.

(9) Pan, C.; Saito, K.; Tanaka, T.; Guo, Q. Low Temperature Growth of In_2O_3 Films via Pulsed Laser Deposition with Oxygen Plasma. *Jpn. J. Appl. Phys.* **2021**, *60*, 055505.

(10) Batzner, S.; Musaelian, A.; Sun, L.; Geiger, M.; Mailoa, J. P.; Kornbluth, M.; Molinari, N.; Smidt, T. E.; Kozinsky, B. E (3)-Equivariant Graph Neural Networks for Data-Efficient and Accurate Interatomic Potentials. *Nat. Commun.* **2022**, *13*, 2453.

(11) Geiger, M.; Smidt, T. E3nn: Euclidean Neural Networks. *arXiv*, 2207.09453, 2022.

(12) Hong, C.; Choi, J. M.; Jeong, W.; Kang, S.; Ju, S.; Lee, K.; Jung, J.; Youn, Y.; Han, S. Training Machine-Learning Potentials for Crystal Structure Prediction Using Disordered Structures. *Phys. Rev. B* **2020**, *102*, 224104.

(13) Kang, Y.; Cho, Y.; Han, S. Cation Disorder as the Major Electron Scattering Source in Crystalline InGaZnO. *Appl. Phys. Lett.* **2013**, *102*, 152104.

(14) Lundstrom, M. *Fundamentals of Carrier Transport*, 2nd ed.; Cambridge University Press; 2000.

(15) Zhang, J.; Wen, X.; Hu, L.; Xu, W.; Zhu, D.; Cao, P.; Liu, W.; Han, S.; Liu, X.; Jia, F.; Zeng, Y.; Lu, Y. C-Axis Oriented Crystalline IGZO Thin-Film Transistors by Magnetron Sputtering. *Journal of Materials Chemistry C* **2017**, *5*, 2388−2396.

(16) Chiang, H. Q.; McFarlane, B. R.; Hong, D.; Presley, R. E.; Wager, J. F. Processing Effects on the Stability of Amorphous Indium Gallium Zinc Oxide Thin-Film Transistors. *J. Non-Cryst. Solids* **2008**, *354*, 2826−2830.

(17) Kamiya, T.; Hosono, H. Material Characteristics and Applications of Transparent Amorphous Oxide Semiconductors. *NPG Asia Materials* **2010**, *2*, 15−22.

(18) Bader, R. F. W. *Atoms in Molecules: A Quantum Theory*; Oxford University Press, New York, 1990.

(19) Henkelman, G.; Arnaldsson, A.; Jónsson, H. A Fast and Robust Algorithm for Bader Decomposition of Charge Density. *Comput. Mater. Sci.* **2006**, *36*, 354−360.

(20) Ma, N.; Tanen, N.; Verma, A.; Guo, Z.; Luo, T.; Xing, H.; Jena, D. Intrinsic Electron Mobility Limits in β-Ga_2O_3. *Appl. Phys. Lett.* **2016**, *109*, 212101.

(21) Smidstrup, S.; Markussen, T.; Vancraeyveld, P.; Wellendorff, J.; Schneider, J.; Gunst, T.; Verstichel, B.; Stradi, D.; Khomyakov, P. A.; Vej-Hansen, U. G.; Lee, M.-E.; Chill, S. T.; Rasmussen, F.; Penazzi, G.; Corsetti, F.; Ojanperä, A.; Jensen, K.; Palsgaard, M. L. N.; Martinez, U.; Blom, A.; Brandbyge, M.; Stokbro, K. QuantumATK: An Integrated Platform of Electronic and Atomic-Scale Modelling Tools. *J. Phys.: Condens. Matter* **2020**, *32*, 015901.

https://doi.org/10.1021/acsmaterialslett.5c00348
ACS Materials Lett. 2025, 7, 2024−2030